Energy Equip. Sys./ Vol. 7/No. 2/June 2019/ 159-173

ENERGY EQUIPSYS

Energy Equipment and Systems

http://energyequipsys.ut.ac.ir
www.energyequipsys.com

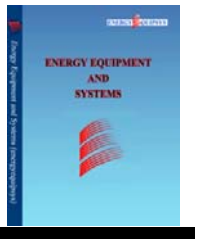

LES/FMDF of premixed methane/air flow in a backward-facing step combustor

Author

Mostafa Esmaeili [a]
Asghar Afshari [b*]

[a] Department of Mechanical Engineering, Faculty of Engineering, Kharazmi University , Tehran, Iran

[b] School of Mechanical Engineering, College of Engineering, University of Tehran, Tehran, Iran

Article history:

Received : 10 January 2019
Accepted : 13 April 2019

ABSTRACT

In the present study, a hybrid Eulerian-Lagrangian methodology is utilized for large eddy simulation (LES) of premixed fuel/air flow over a three-dimensional backward facing step (BFS). The fluid dynamic features are obtained by solving the Eulerian filtered compressible transport equations while the species are predicted by using the filtered mass density function method (FMDF). Some scalar fields are duplicated in FD and MC solvers to examine the numerical consistency between them. A good agreement is achieved by comparing the essential characteristics of the BFS flow (such as the mean and RMS values of the velocity and temperature fields and also the reattachment length) obtained from numerical results with the measurements. This ensures that the proposed hybrid method is reliable for studying the reacting flow in relatively complex combustion systems. Additionally, the performance of several SGS models are assessed, and the results indicate that the dynamic Smagorinsky and WALE models are superior to standard Smagorinsky and MKEV models.

Keywords: Backward Facing Step, Turbulent Reacting Flow, LES, FMDF.

1. Introduction

Regarding its low emissions, lean premixed combustion technology has received much attention in different engineering applications such as gas-based heating and gas turbine power systems. In order to remedy instabilities occurred in these systems[1-3], the geometrical bodies such as bluff-bodies [4] or cylindrical and planar sudden expansions [5] are used to form a recirculating zone for holding the flame and increasing the stability range. Among these types of flame holders, the backward-facing step (BFS) is a simpler configuration in which by recirculation of hot products, the main features of the premixed combustion is preserved.

Turbulent flows over BFS are known to be composed of various flow features. Reattachment, shear layer zone, boundary layers, flow separation and recovery are among such flow regimes [6]. The principal flow features and geometry of the BFS flow are illustrated in Fig. 1.

Because of its extensive application, interesting physics, and its capability to use as a benchmark flow for model validation, the turbulent reacting flow over BFS configuration is focused by many researchers [7-20]. Among them, the experimental studies of Pitz and Daily [13], Ganji and

* Corresponding author: Asghar Afshari
School of Mechanical Engineering, College of Engineering, University of Tehran, Tehran, Iran
Email: afsharia@ut.ac.ir

Sawyer [9], Moreau et al. [11] and El Banhawy et al. [7] comprising a backward facing step as a flame holder, have been simulated by Fureby [8], Park and Ko [12], Kewlani et al. [10] , Shahi et al. [15], Sainte-Rose et al. [14] and Velez et al. [16]. In the study of Sainte-Rose et al. [14], they employed a hybrid LES/RANS approach coupled with a dynamic thickened flame model to simulate premixed methane-air flow over BFS in relatively high Reynolds number of 40000. Their numerical results are compared with the experimental data [11], and they concluded that the separated region results obtained by delayed detached eddy simulation (DDES) model are similar to those of the LES model. Recently, Nemitallah et al. [21] have investigated the effect of equivalence ratio on the turbulent lean-premixed flame stability in a backward-step combustor using LES model. They employed the artificially thickened flame method of OpenFOAM code and showed that by increasing the equivalence ratio, the reattachment length decreases.

Compressible LES methods benefit from a set of density-based governing equations in the filtered form, accompanied by the heat flux and closure subgrid-scale (SGS) models. In the present study, the SGS model is based on the filtered mass density function, commonly known as FMDF, and is utilized in the LES of turbulent reacting flow. This approach was previously used in problems dealing with fundamental aspects of its testing and development. Colucci et al. [22] considered the scalar form of FDF, while Jaberi et al. [23] and many others utilized the scalar FMDF [24-35]. Later, velocity and velocity-scalar FDFs and even velocity scalar FMDF were derived [30, 36-38]. For a better understanding of these concepts, the reader is referred to Givi [39] and Madnia et al. [40]. In this study, LES/LMDF is carried out with the aid of a certain hybrid Eulerian-Lagrangian approach that employs gas dynamic variables based on the Eulerian grid-based field. Moreover, temperature and gaseous species are described via FMDF according to a grid-free Lagrangian field.

In this paper, both turbulent reacting and non-reacting flows over BFS are simulated aided by the hybrid LES/FMDF model which is considered to be a potent method in terms of mathematical and computational capabilities while being able to simulate complicated combustion systems. For this study, regarding premixed methane/air, the LES/FMDF is applied to carry out a simulation on the turbulent flow over BFS.

2. Mathematical formulation and numerical method

The spatial filtering operation[41] is given by

$$\overline{f}(\mathbf{x},t) = \int_{-\infty}^{+\infty} G(\mathbf{x}',\mathbf{x}) f(\mathbf{x}',t) d\mathbf{x}' \tag{1}$$

where G and $\bar{f}(x,t)$ are filter function and transport variable, respectively. The flow variable f is composed of the filtered large scale ($\overline{f}$) and subgrid-scale f_{SGS} parts as

$$f = \overline{f} + f_{SGS}, \tag{2}$$

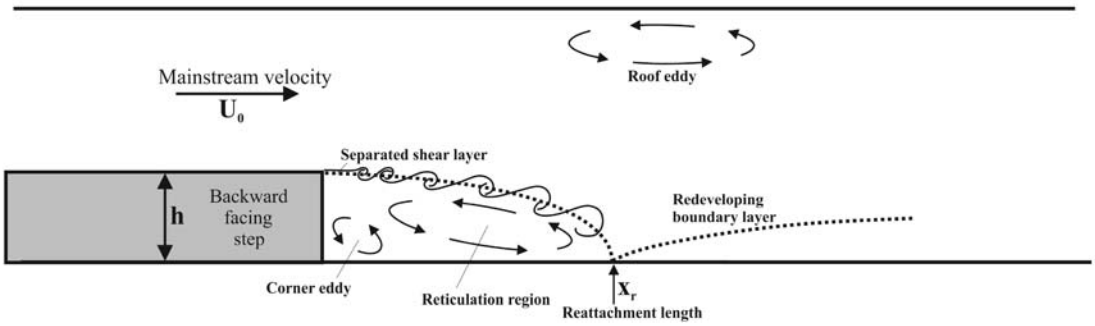

Fig. 1. Flow pattern in BFS flow

Further, in compressible flows, the Favre filtered quantity as

$$\tilde{f} = \frac{\overline{\rho f}}{\bar{\rho}}, \tag{3}$$

is employed. By using the above filter operator, the unsteady, three-dimensional, Favre-filtered, compressible governing equations in a generalized curvilinear coordinates system (ξ_i) can be presented in the following form

$$\frac{\partial \hat{\mathbf{Q}}}{\partial t} + \frac{\partial \hat{\mathbf{E}}_i}{\partial \xi_i} = \frac{1}{J}\hat{\mathbf{S}} \tag{4}$$

where $\hat{S} = \hat{S}(\xi_i, t)$ and $\hat{Q}$ are the source and dependent variables vectors given by

$$\hat{\mathbf{Q}} = \frac{1}{J}\left\{\bar{\rho}, \bar{\rho}\tilde{u}, \bar{\rho}\tilde{v}, \bar{\rho}\tilde{w}, \bar{\rho}\tilde{E}\right\} \tag{5}$$

where the Jacobian of the transformation is defined as

$$J = \partial(\xi, \eta, \zeta, \tau) / \partial(\mathrm{x, y, z, t}) \tag{6}$$

Also, $\hat{\mathbf{E}}_\mathrm{i}$ is the sum of the viscous ($\hat{\mathbf{F}}$) and inviscid ($\hat{\mathbf{D}}_\mathrm{i}$) vectors in generalized coordinates as follows

$$\hat{\mathbf{E}}_i = \hat{\mathbf{F}}_i + \hat{\mathbf{D}}_i \tag{7}$$

$$\hat{\mathbf{F}}_i = \frac{1}{J}\begin{bmatrix} \bar{\rho}\hat{U}_i \\ \bar{\rho}\tilde{u}\hat{U}_i + \bar{p}\dfrac{\partial \xi_i}{\partial x} \\ \bar{\rho}\tilde{v}\hat{U} + \bar{p}\dfrac{\partial \xi_i}{\partial y} \\ \bar{\rho}\tilde{w}\hat{U} + \bar{p}\dfrac{\partial \xi_i}{\partial z} \\ \left(\bar{\rho}\tilde{E} + \bar{p}\right)\hat{U}_i \end{bmatrix} \tag{8}$$

$$\hat{\mathbf{D}}_i = -\frac{1}{J}\begin{bmatrix} 0 \\ \dfrac{\partial \xi_i}{\partial x_j}(\tilde{\tau}_{1j} + \tilde{\tau}_{1j}^{SGS}) \\ \dfrac{\partial \xi_i}{\partial x_j}(\tilde{\tau}_{2j} + \tilde{\tau}_{2j}^{SGS}) \\ \dfrac{\partial \xi_i}{\partial x_j}(\tilde{\tau}_{3j} + \tilde{\tau}_{3j}^{SGS}) \\ \dfrac{\partial \xi_i}{\partial x_j}(-\tilde{q}_j - \tilde{q}_j^{SGS} + (\tilde{\tau}_{jk} + \tilde{\tau}_{jk}^{SGS})\tilde{u}_k) \end{bmatrix} \tag{9}$$

$$\tilde{\tau}_{ij} = \mu\left(\frac{\partial \xi_k}{\partial x_j}\frac{\partial \tilde{u}_i}{\partial \xi_k} + \frac{\partial \xi_k}{\partial x_i}\frac{\partial \tilde{u}_j}{\partial \xi_k} - \frac{2}{3}\delta_{ij}\frac{\partial \xi_k}{\partial x_l}\frac{\partial \tilde{u}_l}{\partial \xi_k}\right) \tag{10}$$

$$\tilde{q}_i = -k\frac{\partial \xi_j}{\partial x_i}\frac{\partial \tilde{T}}{\partial \xi_j} \tag{11}$$

The total energy ($\bar{\rho}\tilde{E}$) is defined as

$$\bar{\rho}\tilde{E} = \bar{\rho}\left\{\tilde{i} + \frac{\tilde{u}^2 + \tilde{v}^2 + \tilde{w}^2}{2}\right\}, \tag{12}$$

and $\tilde{i}$ is the Favre filtered internal energy. Moreover, the dynamic viscosity μ in Eq.(10) is computed using Sutherland's law[42].

The subgrid stress terms which are indicated by SGS superscript are defined as follows

$$\tilde{\tau}_{ij}^{SGS} = \frac{1}{3}\tilde{\tau}_{kk}^{SGS}\delta_{ij} - 2\bar{\rho}\upsilon_t(\tilde{S}_{ij} - \frac{1}{3}\tilde{S}_{kk}\delta_{ij}), \tag{13}$$

where $\tilde{S}_{ij}$ is the strain rate tensor. Based on the low Mach number assumption, the isotropic part of the subgrid stress,$\frac{1}{3}\tilde{\tau}_{kk}^{SGS}$, is neglected [43]. Also, to compute the SGS turbulent viscosity, υ_t, the Smagorinsky model in static [44] and dynamic [45, 46] forms, the WALE model [47], and the MKEV model [22] are employed.

For the Smagorinsky model, the turbulent viscosity is defined as:

$$\upsilon_t = C_d\Delta^2\left|\tilde{S}\right| \tag{14}$$

where $\left|\tilde{S}\right|$ and $\mathrm{C_d}$ are the strain rate tensor magnitude and the model coefficient. Moreover, the SGS heat flux,$\tilde{q}_j^{SGS}$, is defined as

$$\tilde{q}_j^{SGS} = -\frac{\bar{\rho}\upsilon_t}{Pr_t}\frac{\partial \xi_j}{\partial x_j}\frac{\partial \tilde{T}}{\partial \xi_j}, \tag{15}$$

where $\mathrm{Pr_t}$ is the turbulent Prandtl number.

In order to solve the Favre-filtered equations as a Eulerian system (Eq. 4), the higher-order FD approach is employed. The derivatives of the quantities of viscous and inviscid fluxes are computed by the application of the compact-differencing formula of fourth order [48, 49]. In order to keep the tri-diagonal arrangement, one-sided formulas of higher orders are employed at the boundary locations. For time advancement, a low-storage Runge-Kutta scheme is utilized as in [50]. Due to the

increase of numerical errors as the frequencies rise, spatial implicit filtering is used so as to eliminate the generated noise.

To acquire all data regarding the scalar field (temperature and species mass fraction), one should solve the FMDF equation, represented by F_L, in the form

$$\frac{\partial F_L}{\partial t}+\frac{\partial\left[\tilde{u}_i F_L\right]}{\partial x_i}=\frac{\partial}{\partial x_i}\left[(\gamma+\gamma_t)\frac{\partial\left(\frac{F_L}{\bar{\rho}}\right)}{\partial x_i}\right]+\frac{\partial}{\partial \psi_\alpha}\left[\Omega_m\left(\psi_\alpha-\tilde{\phi}_\alpha\right)F_L\right]-\frac{\partial\left[\hat{S}_\alpha F_L\right]}{\partial \psi_\alpha} \quad (16)$$

where Φ is the scalar array, Ψ is the composition domain related to the scalar array and Ω_m is the mixing frequency in the subgrid. It is necessary to solve Eq. (4) using a higher-order Eulerian FD approach so as to obtain the pressure and velocity fields of Eq. (16). Furthermore, the solution of the FMDF equation, Eq. (16), is obtained via the application of a Lagrangian MC method. In this method, the evolution of each MC particle in the physical domain is caused by the joint action of subgrid and molecular diffusivities. It should be noted that FMDF spatial transport is represented by the particle motion using a stochastic differential equation (SDE) in the form [51]

$$dX_i(t)=\left(\sqrt{2(\gamma+\gamma_t)/\bar{\rho}}\right)dW_i(t)+\left(\tilde{u}_i+\frac{1}{\bar{\rho}}\frac{\partial(\gamma+\gamma_t)}{\partial x_i}\right)dt \quad (17)$$

in which W_i denotes the Wiener process and X_i demonstrates the Lagrangian location of a stochastic particle [52]. A particle's compositional value is altered due to the mixing and reaction as explained by an SDE in the form

$$\frac{d\phi_\alpha^+}{\partial t}=-C_\Omega\frac{(\gamma+\gamma_t)}{\bar{\rho}}\left(\phi_\alpha^+-\tilde{\phi}_\alpha\right)+\hat{S}_\alpha\left(\phi^+\right) \quad (18)$$

where $\Phi_a^+=\Phi_a(X(t),t)$ is the particle's scalar value that has a Lagrangian position vector X_i. The data carried by these particles include position and velocity ($x^n(t)$ and $u^n(t)$) along with scalar values ($\Phi^n(t), n=1,\dots,N_p$). Time integration of developed SDEs updates the mentioned parameters. The Eq. 18 can be integrated based on the approximation of Euler-Maruyama [53] as follows

$$x_i^n(t_{k+1})=x_i^n(t_k)+\mathrm{D}_i^n(t_k)\Delta t+E^n(t_k)(\Delta t)^{0.5}\zeta_i^n(t_k) \quad (19)$$

Noteworthy is that the values of the primary four components existing in the vector of the source term, S_0 , in Eq. (4) are all zero, while the value of the fifth component that denotes the source term of reaction belonging to the energy equation is found using a special Arrhenius chemistry model developed for the combustion of methane-air, as presented by Lacaze et al. [54]. A thorough explanation of the LES/FMDF procedure, along with its solution technique, can be found in Afshari et al. [25].

3. Computational Domain Description

In the present study, the computational domain shown in Fig.2 is based on the experimental studies of [11, 14, 55, 56] and its characteristics are described in Table 1. The coordinate directions (*x*, *y* and *z*) shown in the computational domain in Fig.2, represent the streamwise, spanwise, and vertical directions, respectively. The origin of the streamwise axis, x = 0, is taken at the edge of the step. The Reynolds number defined as $Re=\rho U_0 h/\mu$ is set to 40000. The fully turbulent inflow is a premixed methane/air flow with an equivalence ratio of 0.8. The mean inlet velocity is prescribed by a tangent hyperbolic profile with a boundary layer thickness of 0.169h [56]. The velocity profile in the inflow is the sum of the mean velocity and the turbulent velocity perturbations. In the spanwise direction, the periodic boundary condition is applied. Moreover, at the channel exit, a convective boundary condition is used. The no-slip adiabatic boundary condition is applied on the combustor walls.

The multi-block computational domain is composed of two blocks, one in the positive vertical direction (y≥0) and the other in the negative vertical direction (y≤0). Two sets of grids are used in the simulation of the present work. The number of grid points for two meshes is about 0.588×10^6 (coarser grid) and 1.23×10^6 (finer grids). Grid clustering is

introduced near solid walls and in the shear layer downstream of the step. The LES resolution is investigated by using two different approaches. The first approach used to examine the LES resolution is the criterion proposed by Pope [57].

According to this approach, when the turbulent resolution, $M_{pope} = \frac{K_{SGS}}{K_{res}+K_{SGS}}$, is less than 0.2, a well-resolved LES can be obtained. Quantities K_{res} and K_{SGS} are the resolved and the sub-grid scale kinetic energy, respectively.

The number of computational grid points that have various values of the turbulence resolution is illustrated in Fig.3 for two grid arrangements. As can be seen, unlike the coarser grid, for the finer grid, the turbulent resolution is smaller than 0.2 in the entire domain. This confirms that the computational grid distribution in the domain is appropriate, and its resolution is sufficient for LES.

In the second approach for evaluating the adequacy of grid resolution, the effective viscosity (the sum of the fluid and turbulent viscosities) is divided by the fluid viscosity. As discussed by Coussement et al. [58], for the LES computations, this ratio must be below 10. The number of computational grid points that have various values of υ_{eff}/υ, computed for reacting BFS flow, are shown in Fig.4. Obviously, the viscosity ratio for most of the cells is less than 2, which ensures that the grid is appropriate for LES computations, and the large scale flow structures are properly resolved.

4. Results and discussion

The BFS configuration studied here is based on the experimental study of [11, 55]. In these studies, the turbulent premixed flame stabilized at the behind of the BFS with the expansion ratio of 1.538 is considered. The main characteristics of the computational domain and inflow condition are listed in Table 1. Here, the simulations are carried out for non-reacting ($\Phi=0$) and reacting ($\Phi=0.8$) premixed methane/air flow. To analysis the recirculating zone, the mean reattachment length obtained by using different SGS models are compared with the published numerical and experiment data [11, 14, 56]. It is noticeable that the predicted value of the mean reattachment length using all SGS models lies in the experimental reported range. The value obtained by Smagorinsky (C_d=0.014) model is towards the lower limit of the experimental length while for the MKEV model, it tends to the upper bound. Also, the reattachment length obtained by MKEV model is so close to the DDES computations of Sainte-Rose et al. [14], which better predicted the reattachment length in comparison to the LES model. Moreover, for the RANS model, their computations are clearly overestimated.

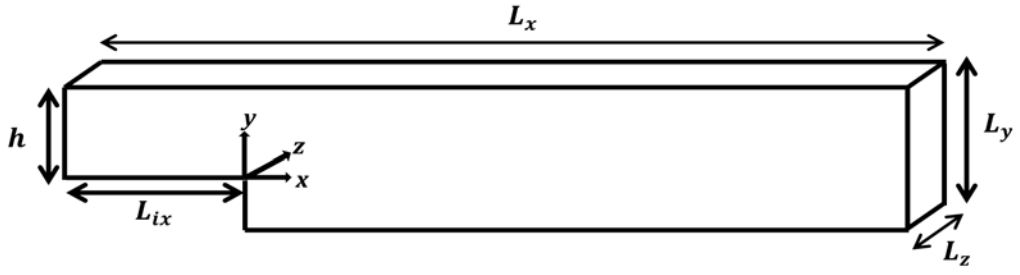

Fig.2.Sketch of the computational domain

Table 1. The characteristics of the computational domain and the inflow boundary condition

Computational domain				Inflow		
L_x	L_{ix}	L_y	L_z	Re_h	T_i (K)	Equivalence ratio
23h	3h	2.857h	2h	40000	520	0.8

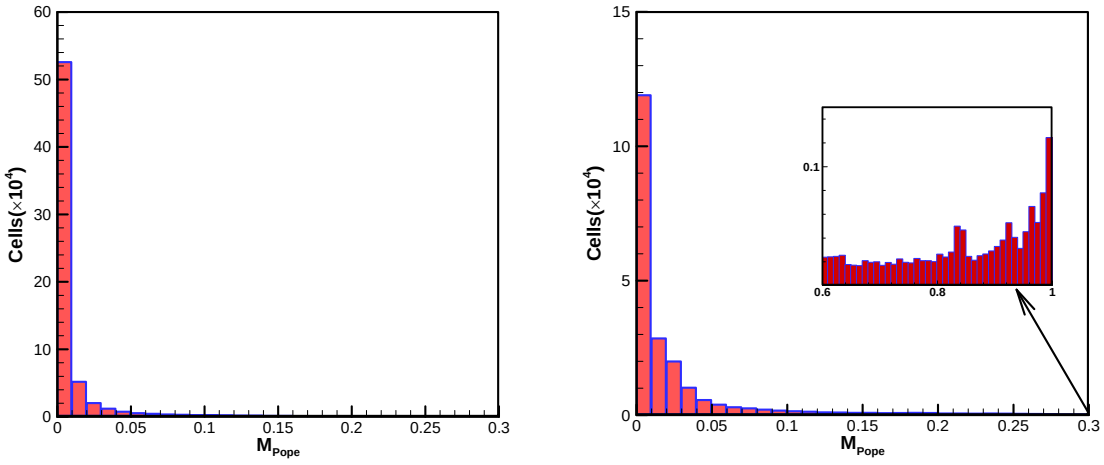

Fig.3. The number of grid points that have various values of the Mpope in BFS flow; (a) fine grid (b) coarse grid

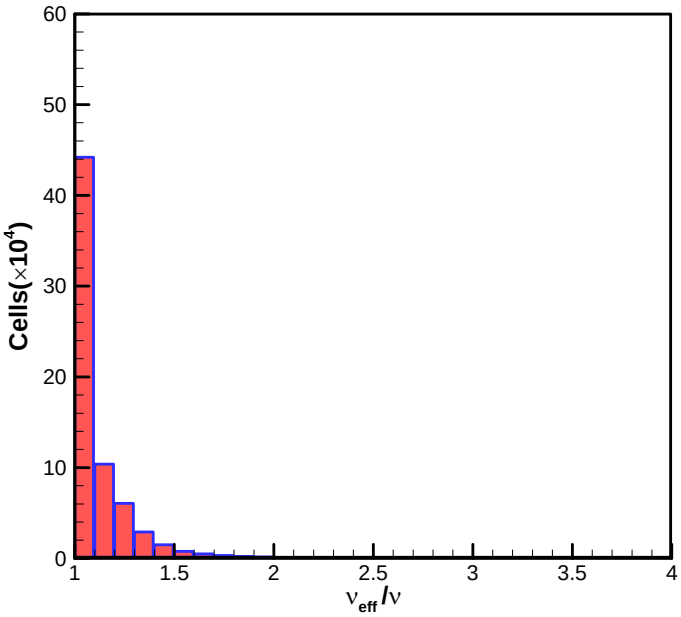

Fig.4. The number of grid points that have various values of viscosity ratio in BFS flow simulation with a fine grid

Mean streamlines obtained from LES computation for non-reacting flow using different SGS model together with the LES results of Sainte-Rose et al. [14] are demonstrated in Fig.5. As shown, apart from the large primary recirculation zone, there is a secondary bubble in the step corner. As a major difference between confined and unconfined BFS, depending on the Reynolds number, a secondary separated region (roof vortex) can be observed in confined BFS flow. It is as a result of the sudden expansion at the edge of the step leading to an adverse pressure gradient [59].

For the BFS flow with the mentioned Reynolds number and other geometrical conditions (Table 1), the secondary recirculating zone is not observed experimentally [11, 55]. As shown in Fig.5, in the result obtained using the Smagorinsky (C_d=0.014) model, a large separated region are formed near the upper wall, which may be due to the incorrect limiting behavior of this model near the wall. Similar to the LES result of

Sainte-Rose et al. [14], this secondary separated region is getting so smaller for DSM and WALE models. To more explanation, the effect of SGS modeling on the mean streamwise velocity at two different locations (one is near the step and the other is in the secondary separated region) are shown in Fig.6. In the location of x/h=0.57, all models similarly follow the experimental data trend, but at x/h=6, MKEV and Smagorinsky (Cd=0.014) models fail to predict the near wall behavior leading to a large secondary recirculation zone.

Figure 7 and Fig.8 , respectively, present comparison of the mean and fluctuating streamwise velocity profiles with those of experimental data [11, 55] in six streamwise locations for non-reacting flow. The computed results, obtained by using the DSM SGS model, are in a good agreement with the experiment. The mixing layer growth and thickness are precisely predicted by our numerical results.

Table 2. The reattachment length behind BFS for non-reacting flow: comparison between present results and numerical and experimental studies of [11, 14, 56]

		Reattachment length
Experimental data of [11]		4.3h<-<6h
RANS Study of Sainte-Rose et al. [14, 56]		7.8h
LES Study of Sainte-Rose et al. [14, 56]		4.1h
DDES Study of Sainte-Rose et al. [14, 56]		5.1h – 5.3h
Present LES simulation	Smagorinsky (C_d=0.014)	4.69h
	MKEV	5.17h
	DSM	4.8h
	WALE	4.905h

(a) Smagorinsky (C_d=0.014)

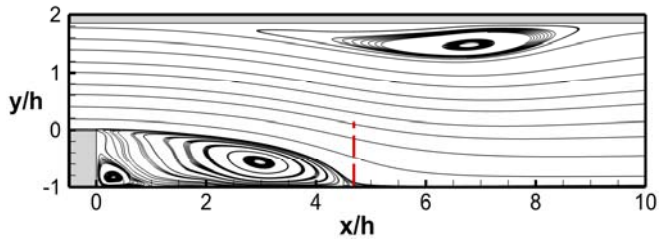

(b) MKEV

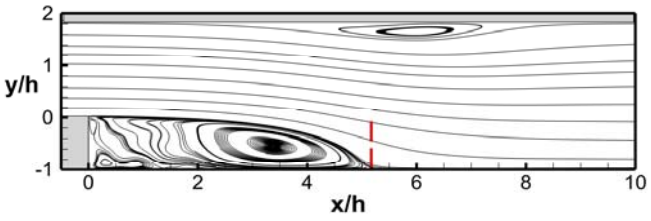

(c) DSM

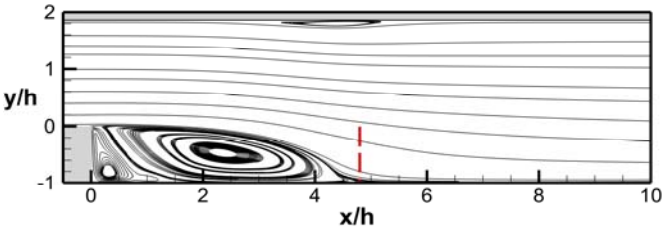

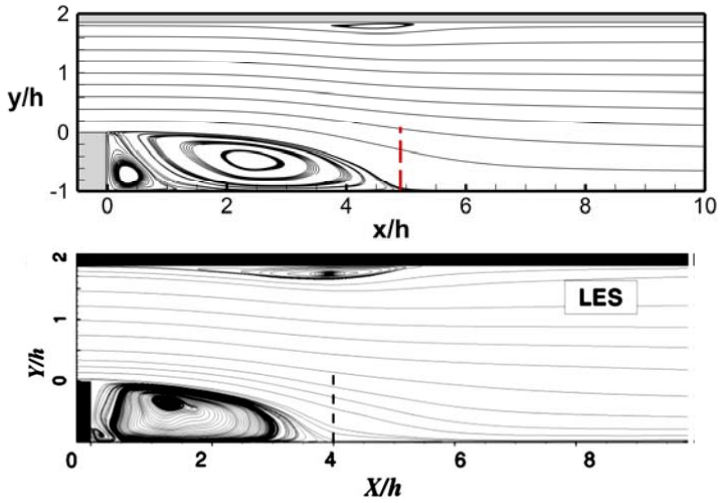

Fig. 5. Average streamlines obtained from LES computation by different SGS closure

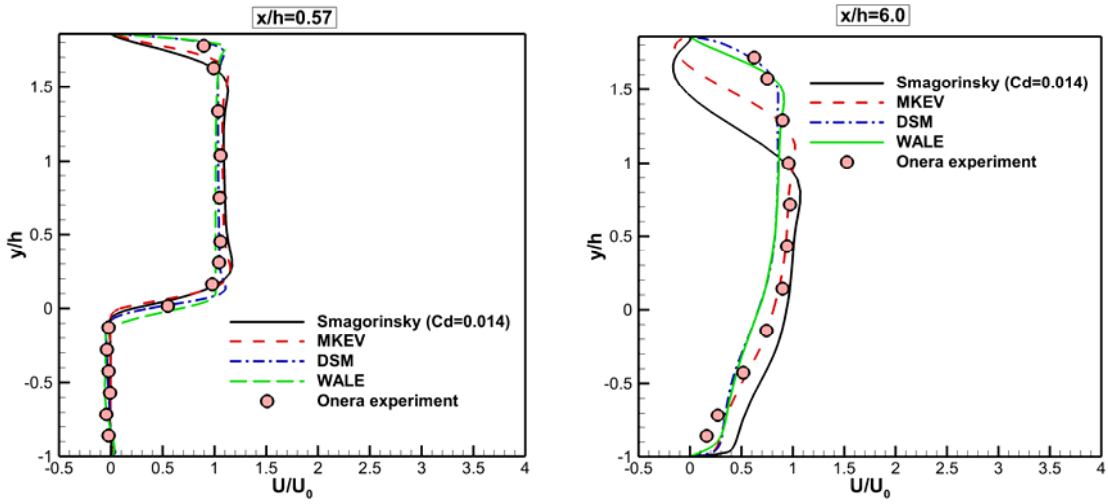

Fig. 6. Comparison between mean streamwise velocities obtained from numerical results and experimental data. (a) x/h=0, (b)x/h=6

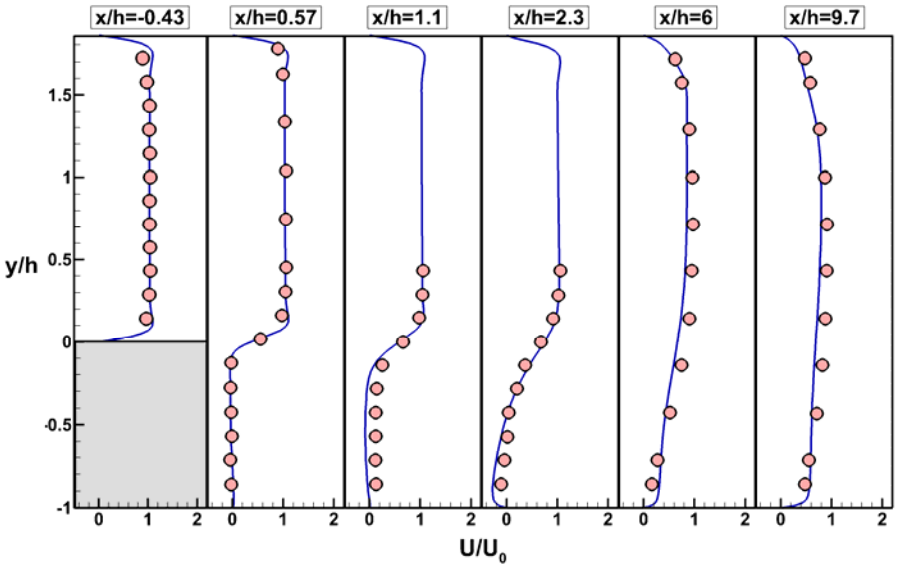

Fig. 7. Comparison of the mean streamwise velocity profile for non-reacting flow (Φ=0); present computation (solid line) and experimental data(symbol)

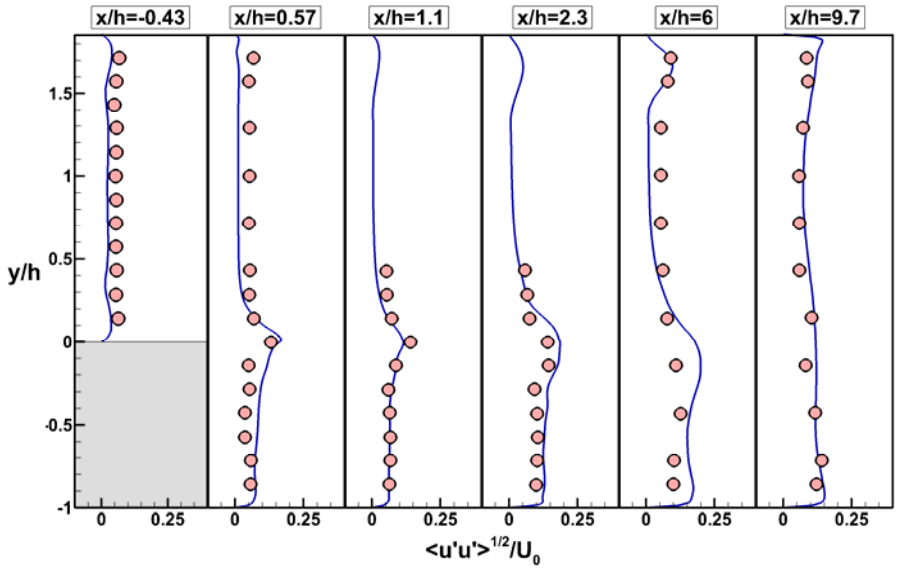

Fig. 8. Comparison of (a) mean and (b) fluctuating streamwise velocity profile for non-reacting flow (Φ=0); present computation (solid line) and experimental data(symbol)

Following is the reacting BFS flow analysis. To investigate the numerical accuracy, one should evaluate the consistency of Lagrangian FMDF-MC data as well as Eulerian LES-FD data for the reacting BFS flow where the changes in density and temperature are substantial. To this end, the LES-FD and FMDF-MC scalars are compared. In Fig. 9(a) and Fig. 9(b), the instantaneous filtered temperature fields computed by FD and MC solvers are compared. As shown, the solvers similarly resolve the temperature variations in the reacting BFS flow. It establishes that FD and MC solvers are numerically accurate. Temperature distribution also shows that there is a noticeable amount of the unburned hydrocarbon at the combustor outflow. It can be better explained by the heat release contour (Fig. 9 (c)).

According to earlier findings regarding non-reacting flow, to model SGS stress, one should benefit from the DSM SGS model as it

provides the most realistic predictions for the flow. The averaged velocity results for the LES\FMDF computations are presented first. In Table 3, the obtained numerical results for reattachment length are compared with the available experimental and numerical data [11, 14, 56]. The computed reattachment length is excellently matched to lower bound of the experimental data while for other published numerical data; this separated region length is overestimated. It is worthy to note that the reattachment length decreases by 38.5% compared to the non-reacting flow as a result of the expansion caused by the combustion [15]. This shortened length is shown in Fig.10, in which averaged streamlines for reacting BFS flow is provided.

To assess the combustion process impact on the mean flow field, one can refer to the profiles of stream-wise velocity in the reacting flow, as shown in various streamwise locations in Fig. 11. As can be seen, a good agreement exists between empirical and numerical findings. Compared to the experimental data, the velocity profile is underestimated to some extent in the y/h<0 region. This is more pronounced in the location of x/h=4.3, where the predicted reverse flow is lower than that of the experiment. It should be noted that as a result of heat release, in comparison to non-reacting flow, the maximum reverse flow velocity in the reacting flow is higher.

Here, the results obtained for the time-averaged temperature flow-field is considered. In Fig.12, a $T = 1500\ K$ iso-line is demonstrated for the present computations and compared to the temperature measurements [55]. The approximate location of the time-averaged flame can be found from this figure. This figure represents the approximate position of the time-averaged flame. Near the step, the computed flame is closely matched to the experimental data. In the further downstream, the flame angle is overpredicted by the present computations. This discrepancy can be attributed to the high levels of the velocity fluctuations for the LES computation. Considering the mean temperature profiles in Fig.13, a good agreement between the LES/FMDF and experimental data is observed confirming the ability of the hybrid methodology used in the present study. Only in the first and last profile, some discrepancies from experimental data are seen. In Fig.14, the fluctuating temperature profile is compared with experimental data. In three first locations, the overall agreement is good and computed results properly reproduce the peak and level of fluctuating temperature, but in the last three, numerical results approximately follow the trend of the experiment. In the first three locations, the peak and level of fluctuating temperature are in very good agreement with the experiments, but in the last three, numerical results approximately follow the trend of the experiment.

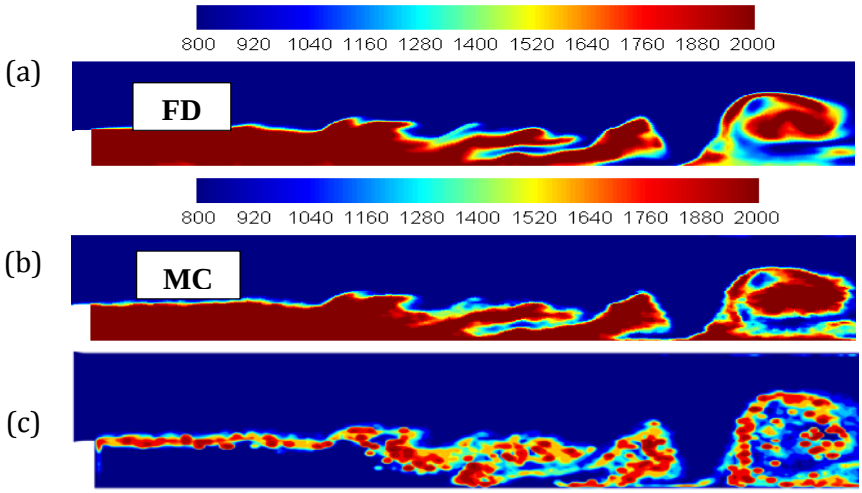

Fig. 9. The instantaneous filtered temperature distribution for the reacting BFS flow by using (a) FD and (b)MC solutions. The instantaneous distribution of the heat release (c)

Table 3. The reattachment length behind BFS for reacting flow: comparison between present results and numerical and experimental studies of [11, 14, 56].

	Reattachment length
Experimental work [11]	2.9h<-<3.4h
RANS Study of Sainte-Rose et al. [14, 56]	4.7h
LES Study of Sainte-Rose et al. [14, 56]	3.6h
DDES Study of Sainte-Rose et al. [14, 56]	3.8h
Present LES simulation	2.95h

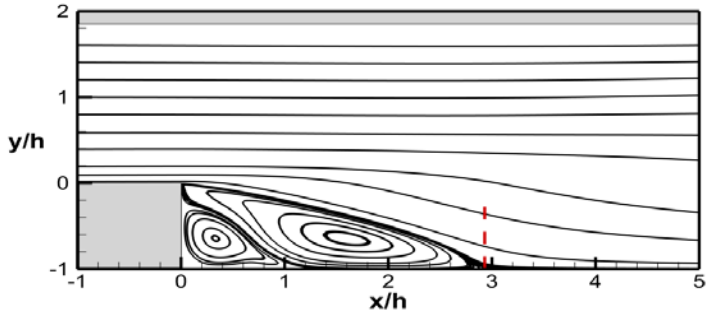

Fig. 10. Average streamlines behind step for reacting flow (Φ=0.8)

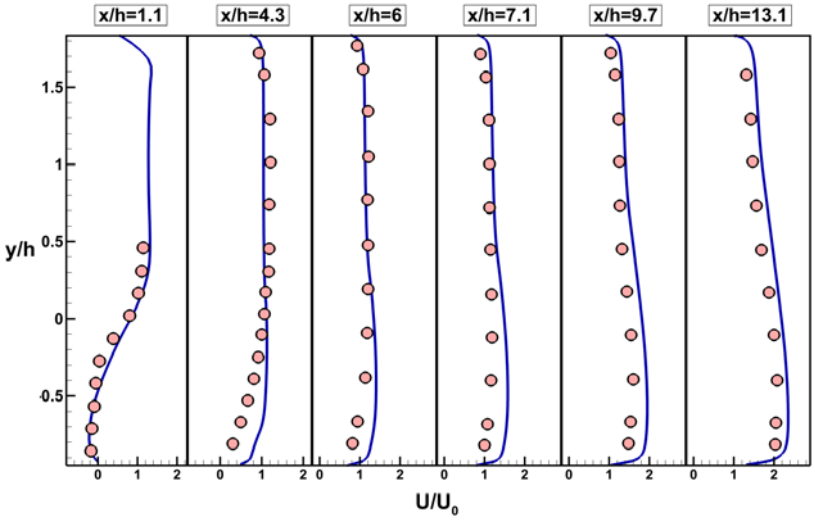

Fig. 11. Comparison of the mean streamwise velocity profile for reacting flow (Φ=0.8); present computation (solid line) and experimental data (symbol)

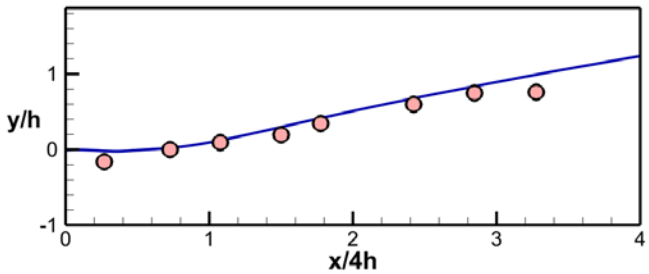

Fig. 12. Mean temperature iso-line (1500 K); present computation (solid line) and experimental data (symbol)

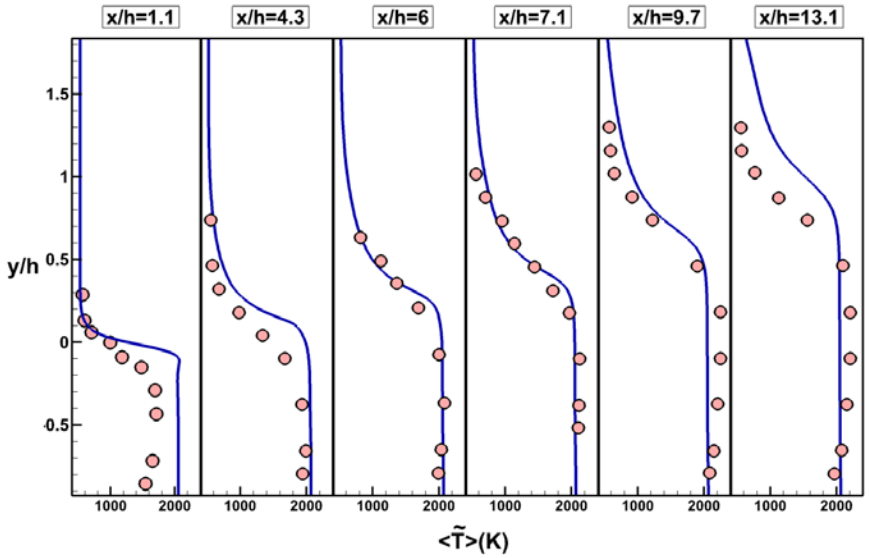

Fig. 13. Comparison of mean temperature profile for reacting flow (Φ=0.8); present computation (solid line) and experimental data (symbol)

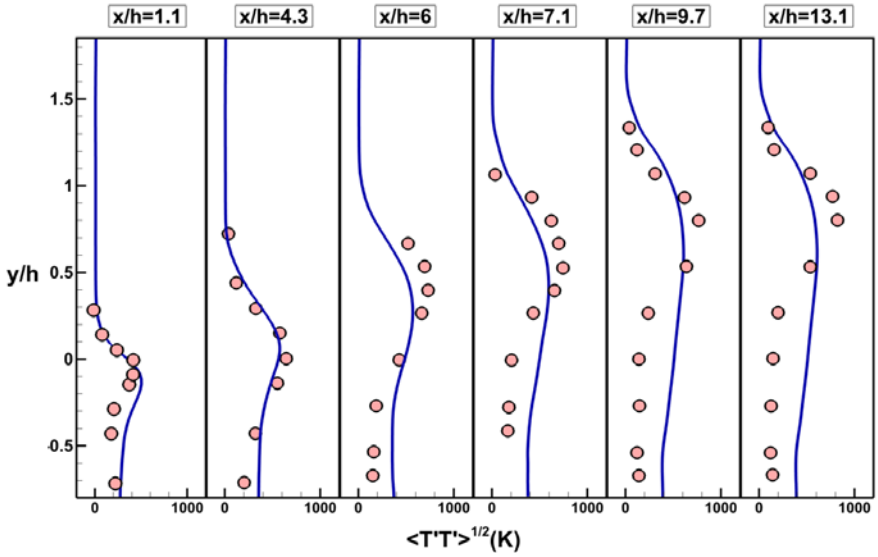

Fig. 14. Comparison of fluctuating temperature profile for reacting flow (Φ=0.8); present computation (solid line) and experimental data (symbol)

5.Conclusion

In the present article, the LES/FMDF approach is employed to simulate the turbulent reacting flow over BFS. In the first step, a comprehensive discussion is presented on the efficacy of LES modeling with regard to the characteristics of turbulent flow over BFS when no reaction occurs. Next, the LES/FMDF approach is utilized to carry out the calculations for the reacting flow. A satisfactory consistency between the Lagrangian MC and Eulerian FD components of the hybrid model of LES/FMDF is demonstrated. The results obtained via the LES/FMDF approach are compared with those obtained via the measured data and a good agreement is shown. Accordingly, the provided procedure is able to accurately model the flow and combustion related to the BFS configuration. Different SGS models are used in this paper, and the results obtained by the DSM and WALE SGS models are closer to the measurements. The obtained results precisely

reproduce the main characteristics of the reacting and non-reacting turbulent BFS flow such as the reattachment length, turbulent statistics and high turbulence shear layer and the flame angle and its location.

References

[1] H.M. Altay, D.E. Hudgins, R.L. Speth, A.M. Annaswamy, A.F. Ghoniem, Mitigation of thermoacoustic instability utilizing steady air injection near the flame anchoring zone, Combustion and Flame, 157(4) (2010) 686-700.

[2] H.M. Altay, R.L. Speth, D.E. Hudgins, A.F. Ghoniem, Flame–vortex interaction driven combustion dynamics in a backward-facing step combustor, Combustion and Flame, 156(5) (2009) 1111-1125.

[3] T. Kitano, K. Kaneko, R. Kurose, S. Komori, Large-eddy simulations of gas- and liquid-fueled combustion instabilities in back-step flows, Combustion and Flame, 170 (2016) 63-78.

[4] W. Jones, A. Marquis, F. Wang, Large eddy simulation of a premixed propane turbulent bluff body flame using the Eulerian stochastic field method, Fuel, 140 (2015) 514-525.

[5] Y. Huang, V. Yang, Dynamics and stability of lean-premixed swirl-stabilized combustion, Progress in Energy and Combustion Science, 35(4) (2009) 293-364.

[6] D.M. Driver, H.L. Seegmiller, J.G. Marvin, Time-dependent behavior of a reattaching shear layer, AIAA Journal, 25(7) (1987) 914-919.

[7] Y. El Banhawy, S. Sivasegaram, J. Whitelaw, Premixed, turbulent combustion of a sudden-expansion flow, Combustion and Flame, 50 (1983) 153-165.

[8] C. Fureby, Homogenization based LES for turbulent combustion, Flow, turbulence and combustion, 84(3) (2010) 459-480.

[9] A. Ganji, R. Sawyer, Experimental study of the flow field of a two-dimensional premixed turbulent flame, AIAA Journal, 18(7) (1980) 817-824.

[10] G. Kewlani, K. Vogiatzaki, S. Shanbhogue, A.F. Ghoniem, Validation Study of Large-Eddy Simulations of Wake Stabilized Reacting Flows using Artificial Flame Thickening Approaches, in: 51st AIAA Aerospace Sciences Meeting including the New Horizons Forum and Aerospace Exposition, 2013.

[11] P. Moreau, J. Labbe, F. Dupoirieux, R. Borghi, Experimental and numerical study of a turbulent recirculation zone with combustion, in: Turbulent Shear Flows 5, Springer, 1987, pp. 337-346.

[12] N.S. Park, S.C. Ko, Large eddy simulation of turbulent premixed combustion flows over backward facing step, Journal of mechanical science and technology, 25(3) (2011) 713-719.

[13] R.W. Pitz, J.W. Daily, Combustion in a turbulent mixing layer formed at a rearward-facing step, AIAA Journal, 21(11) (1983) 1565-1570.

[14] B. Sainte-Rose, N. Bertier, S. Deck, F. Dupoirieux, A DES method applied to a Backward Facing Step reactive flow, Comptes Rendus Mécanique, 337(6) (2009) 340-351.

[15] M. Shahi, J.B. Kok, A. Pozarlik, On characteristics of a non-reacting and a reacting turbulent flow over a backward facing step (BFS), International Communications in Heat and Mass Transfer, 61 (2015) 16-25.

[16] C. Velez, S. Martin, A. Jemcov, S. Vasu, Large Eddy Simulation of an Enclosed Turbulent Reacting Methane Jet With the Tabulated Premixed Conditional Moment Closure Method, Journal of Engineering for Gas Turbines and Power, 138(10) (2016) 101501.

[17] S. Hemchandra, S. Shanbhogue, S. Hong, A.F. Ghoniem, Role of hydrodynamic shear layer stability in driving combustion instability in a premixed propane-air backward-facing step combustor, Physical Review Fluids, 3(6) (2018) 063201.

[18] B.S. Long, A.M. Briones, S.D. Stouffer, B.A. Rankin, Effect of Rayleigh-Taylor Instability on Backward-Facing-Step Stabilized Turbulent Premixed Flames, in: ASME Turbo Expo 2017:

Turbomachinery Technical Conference and Exposition, American Society of Mechanical Engineers, 2017, pp. V04BT04A027-V004BT004A027.

[19] B. Nagarajan, N. Baraiya, S. Chakravarthy, Effect of inlet flow turbulence on the combustion instability in a premixed backward-facing step combustor, Proceedings of the Combustion Institute, (2018).

[20] R. Sampath, M. Mathur, S.R. Chakravarthy, Lagrangian coherent structures during combustion instability in a premixed-flame backward-step combustor, Physical Review E, 94(6) (2016) 062209.

[21] M.A. Nemitallah, G. Kewlani, S. Hong, S.J. Shanbhogue, M.A. Habib, A.F. Ghoniem, Investigation of a turbulent premixed combustion flame in a backward-facing step combustor; effect of equivalence ratio, Energy, 95 (2016) 211-222.

[22] P. Colucci, F. Jaberi, P. Givi, S. Pope, Filtered density function for large eddy simulation of turbulent reacting flows, Physics of Fluids (1994-present), 10(2) (1998) 499-515.

[23] F. Jaberi, P. Colucci, S. James, P. Givi, S. Pope, Filtered mass density function for large-eddy simulation of turbulent reacting flows, Journal of Fluid Mechanics, 401 (1999) 85-121.

[24] A. Afshari, F. Jaberi, LARGE-SCALE SIMULATIONS OF TURBULENT COMBUSTION AND PROPULSION SYSTEMS, in: G.D. Roy (Ed.) Combustion Processes in Propulsion: Control, Noise, and Pulse Detonation, Academic Press, 2005, pp. 31.

[25] A. Afshari, F.A. Jaberi, T.I. Shih, Large-eddy simulations of turbulent flows in an axisymmetric dump combustor, AIAA Journal, 46(7) (2008) 1576-1592.

[26] A. Banaeizadeh, Z. Li, F.A. Jaberi, Compressible Scalar Filtered Mass Density Function Model for High-Speed Turbulent Flows, AIAA Journal, 49(10) (2011) 2130-2143.

[27] F.A. Jaberi, Large eddy simulation of turbulent pre-mixed flame via filtered mass density function, in: 37th AIAA Aerospace Sciences Meeting and Exhibit, 1999.

[28] S. James, F. Jaberi, Large scale simulations of two-dimensional nonpremixed methane jet flames, Combustion and Flame, 123(4) (2000) 465-487.

[29] M. Nik, S. Yilmaz, P. Givi, M. H. Sheikhi, S. Pope, Simulation of Sandia flame D using velocity-scalar filtered density function, AIAA Journal, 48(7) (2010) 1513-1522.

[30] M. Sheikhi, T. Drozda, P. Givi, F. Jaberi, S. Pope, Large eddy simulation of a turbulent nonpremixed piloted methane jet flame (Sandia Flame D), Proceedings of the Combustion Institute, 30(1) (2005) 549-556.

[31] M. Yaldizli, K. Mehravaran, F. Jaberi, Large-eddy simulations of turbulent methane jet flames with filtered mass density function, International Journal of Heat and Mass Transfer, 53(11) (2010) 2551-2562.

[32] S.L. Yilmaz, M. Nik, P. Givi, P.A. Starkey, Scalar filtered density function for large eddy simulation of a Bunsen burner, Journal of Propulsion and Power, 26(1) (2010) 84-93.

[33] M. Esmaeili, A. Afshari, F.A. Jaberi, Large-eddy simulation of turbulent mixing of a jet in cross-flow, Journal of Engineering for Gas Turbines and Power, 137(9) (2015) 091510.

[34] M. Esmaeili, A. Afshari, F.A. Jaberi, Turbulent mixing in a non-isothermal jet in crossflow, International Journal of Heat and Mass Transfer, 89 (2015) 1239-1257.

[35] A. Banaeizadeh, A. Afshari, H. Schock, F. Jaberi, Large-eddy simulations of turbulent flows in internal combustion engines, International Journal of Heat and Mass Transfer, 60 (2013) 781-796.

[36] M. Sheikhi, P. Givi, S. Pope, Velocity-scalar filtered mass density function for large eddy simulation of turbulent reacting flows, Physics of Fluids (1994-present), 19(9) (2007) 095106.

[37] L.Y. Gicquel, P. Givi, F. Jaberi, S. Pope, Velocity filtered density function for large eddy simulation of turbulent flows, Physics of Fluids (1994-present), 14(3) (2002) 1196-1213.

[38] M. Sheikhi, T. Drozda, P. Givi, S. Pope, Velocity-scalar filtered density function for large eddy simulation of

turbulent flows, Physics of Fluids (1994-present), 15(8) (2003) 2321-2337.
[39] P. Givi, Filtered density function for subgrid-scale modeling of turbulent combustion, AIAA Journal, 44(1) (2006) 16-23.
[40] C.K. Madnia, F.A. Jaberi, P. Givi, Large eddy simulation of heat and mass transport in turbulent flows, Handbook of Numerical Heat Transfer, Second Edition, (2006) 167-189.
[41] A.A. Aldama, Filtering techniques for turbulent flow simulation, Springer Science & Business Media, 2013.
[42] W. Sutherland, LII. The viscosity of gases and molecular force, The London, Edinburgh, and Dublin Philosophical Magazine and Journal of Science, 36(223) (1893) 507-531.
[43] J. Suh, S.H. Frankel, L. Mongeau, M.W. Plesniak, Compressible large eddy simulations of wall-bounded turbulent flows using a semi-implicit numerical scheme for low Mach number aeroacoustics, Journal of Computational Physics, 215(2) (2006) 526-551.
[44] A. Yoshizawa, Statistical theory for compressible turbulent shear flows, with the application to subgrid modeling, Physics of Fluids (1958-1988), 29(7) (1986) 2152-2164.
[45] M. Germano, U. Piomelli, P. Moin, W.H. Cabot, A dynamic subgrid-scale eddy viscosity model, Physics of Fluids A: Fluid Dynamics (1989-1993), 3(7) (1991) 1760-1765.
[46] P.a. Moin, K. Squires, W. Cabot, S. Lee, A dynamic subgrid-scale model for compressible turbulence and scalar transport, Physics of Fluids A: Fluid Dynamics (1989-1993), 3(11) (1991) 2746-2757.
[47] F. Nicoud, F. Ducros, Subgrid-scale stress modeling based on the square of the velocity gradient tensor, Flow, Turbulence and Combustion, 62(3) (1999) 183-200.
[48] S.K. Lele, Compact finite difference schemes with a spectral-like resolution, Journal of computational physics, 103(1) (1992) 16-42.
[49] M.R. Visbal, D.V. Gaitonde, Very high-order spatially implicit schemes for computational acoustics on curvilinear meshes, Journal of Computational Acoustics, 9(04) (2001) 1259-1286.
[50] S. Gottlieb, C.-W. Shu, E. Tadmor, Strong stability-preserving high-order time discretization methods, SIAM Review, 43(1) (2001) 89-112.
[51] C. Gardiner, Handbook of stochastic methods, Springer-Verlag, New York, 1990.
[52] S. Karlin, H.M. Taylor, A second course in stochastic processes, Gulf Professional Publishing, 1981.
[53] P.E. Kloeden, E. Platen, Numerical solution of stochastic differential equations, Springer, 1992.
[54] G. Lacaze, E. Richardson, T. Poinsot, Large eddy simulation of spark ignition in a turbulent methane jet, Combustion and Flame, 156(10) (2009) 1993-2009.
[55] P. Magre, G. Collin, P. Bouchardy, Application de la DRASC á l'opération A3C, Onera Technical Report - RTS 4/3608 EY, (1992).
[56] B. Sainte-Rose, Simulations numériques d'écoulements réactifs massivement décollés par une approche hybride RANS/LES, Châtenay-Malabry, Ecole centrale de Paris, 2010.
[57] S.B. Pope, Ten questions concerning the large-eddy simulation of turbulent flows, New Journal of Physics, 6(1) (2004) 35.
[58] A. Coussement, O. Gicquel, G. Degrez, Large Eddy Simulation of a Pulsed Jet in Crossflow, in: Proceedings of the 48th AIAA Aerospace Sciences Meeting Including the New Horizons Forum and Aerospace Exposition, 2010.
[59] G. Biswas, M. Breuer, F. Durst, Backward-facing step flows for various expansion ratios at low and moderate Reynolds numbers, Journal of fluids engineering, 126(3) (2004) 362-374.